Integration of surface geophysical methods for fracture detection in crystalline bedrocks of southwestern Nigeria

A. A. Adepelumi · M. -J. Yi · J. -H. Kim · B. D. Ako · J. S. Son

Abstract The application of electrical imaging and very low frequency (VLF) electromagnetics was investigated for the purpose of delineating basement fracture zones, and to show how incorporating a priori information in numerical modelling would facilitate the location of fractured zones within a basement rock more precisely. To this end, direct current (DC) dipole–dipole resistivity and VLF modelling and inversion experiments were carried out to evaluate the efficacy of the methods in detecting low-resistivity fracture zones in a typical crystalline basement rock that is favourable for groundwater accumulation. Most wells drilled in such an environment usually have low yields. Results of the numerical experiment generally indicate that fractures covered by moderate overburden, and having considerable depth, extent, and thickness compared to the depth of fracture burial, produce good responses resulting in high-resolution resistivity images. Lower resolution resistivity images were obtained as the thickness of the overburden increased. Also, the model investigations indicate that width of the fracture zone plays a major role in controlling image resolution. Conclusions from the synthetic modelling were confirmed by resistivity and VLF data gathered across a suspected fault in a hard rock terrain of southwestern Nigeria. The results from the field data are in general agreement with the numerical modelling experiments.

Received: 2 November 2004 / Accepted: 30 March 2006
Published online: 20 June 2006

Integración de métodos geofísicos superficiales para la detección de fracturas en macizos rocosos cristalinos del suroeste de Nigeria.

A. A. Adepelumi (✉) · M. -J. Yi · J. -H. Kim · J. S. Son
Korea Institute of Geoscience and Mineral Resources,
30 Kajung-dong Yusung-gu, 305-350, Daejeon, South Korea
e-mail: adepelumi@yahoo.co.uk
Tel.: +82-42-8683171
Fax: +82-42-8619721

A. A. Adepelumi · B. D. Ako
Department of Geology,
Obafemi Awolowo University,
Ile-Ife, Osun State, Nigeria

Résumé L'application de l'imagerie électrique et de l'électromagnétique à très basse fréquence (VLF), a été évaluée pour la localisation de zones de fractures de socle, et pour montrer comment l'incorporation de ce type d'information dans un modèle numérique peut faciliter la localisation plus précise des zones de fractures dans le socle. A cet effet, la résistivité par Courant Directe (DC en anglais) dipôle-dipôle, la modélisation des résultats du VLF et des essais d'inversion ont été réalisés pour évaluer la rentabilité de ces méthodes sur un socle cristallin typique et faorable à l'accumulation des eaux souterraines. La plus part des puits réalisés dans ces environnement présentent des débits faibles. Les résultats d'expériences numériques indiquent généralement que les fractures recouvertes par de fines formations de surface, et possédant une profondeur, épaisseur et extension importantes comparées à la profondeur d'enfouissement, produisent de meilleures réponses sur des images de résistivité de haute résolution. Les images de plus basses résolutions sont obtenues lorsque la couverture de surface diminue. Les conclusions du modèle intial ont été confirmées par les données de résistivité et le VLF, collectées à travers une faille suspectée dans un terrain de socle du Sud-Ouest du Nigeria. Les résultats des données de terrain sont en général en accordance avec les modélisations numériques.

Resumen Se investigó la aplicación de imágenes eléctricas y electromagnéticas de muy baja frecuencia (VLF) con el objetivo de delimitar zonas de fractura en el basamento y de mostrar como la incorporación de información a priori en modelos numéricos facilitaría la localización con mayor precisión de zonas de fractura dentro de rocas del basamento. Con este objetivo se llevaron a cabo experimentos de inversión y modelizado en corriente directa (DC), resistividad dipolo-dipolo, y VLF para evaluar la eficacia de los métodos en la detección de zonas de fractura de baja resistividad en rocas típicas del basamento que son favorables para la acumulación de agua subterránea. La mayoría de pozos que se han perforado en este tipo de ambiente tienen bajas productividades. Los resultados del experimento numérico generalmente indican que las fracturas cubiertas por material residual, y que tienen considerable profundidad, espesor, y extensión en comparación con la profundidad a que está enterrada la fractura, producen buenas respuestas

 DOI 10.1007/s10040-006-0051-2

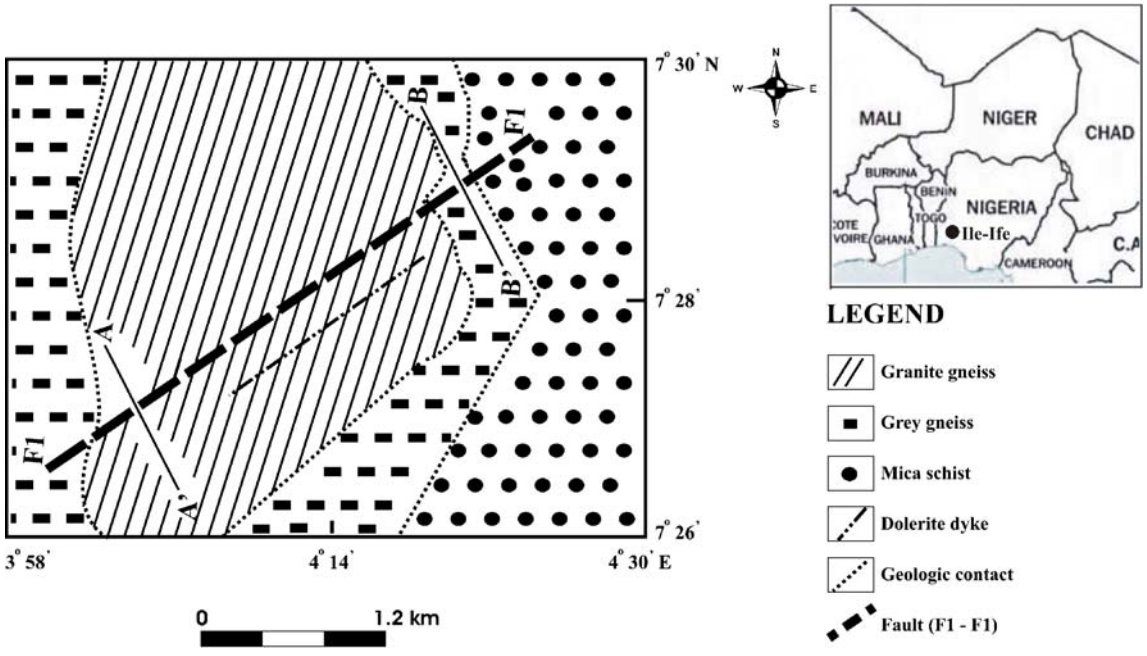

Fig. 1 Geological map of the survey site at Ile-Ife, showing the location of the suspected fault and profiles A-A′ and B-B′ used for data

dando por resultado imágenes de resistividad de alta resolución. Se obtuvieron imágenes de resistividad de baja resolución a medida que el espesor del material residual incrementaba. Las investigaciones del modelo también indican que el ancho de la zona de fractura juega un papel principal en el control de la resolución de la imagen. Las conclusiones del modelizado sintético se confirmaron con datos de campo de resistividad y VLF obtenidos a través de una supuesta falla en un terreno de rocas duras del suroeste de Nigeria. Los resultados de campo concuerdan muy bien con los experimentos de modelizado numérico.

Keywords Electrical resistivity · Very low frequency electromagnetics (VLF) · Groundwater exploration · Fractured rocks · Basement

Introduction

A pilot shallow electrical resistivity survey and numerical modelling experiment was undertaken to explore the efficacy of direct current (DC) dipole–dipole resistivity and very low frequency (VLF) electromagnetic methods in detecting the fractures/faults zone beneath a relatively thick overburden within the crystalline basement rocks of Ile-Ife, southwestern Nigeria. The study was conducted to proffer solutions regarding the occurrence of acute water supply shortage in most of the crystalline bedrock environments of southwestern Nigeria. This shortage is due to collapse of many public water systems in most cities, and increasing demand resulting from increase in rural to urban migration of the people. Borehole yield is frequently low in the Ile-Ife area during the dry season and, during this period, water supplies from boreholes do not have long-term sustainability, so it is imperative to locate boreholes within the fractured and/or faulted basement rocks that are ubiquitous in this area. Detecting the locations of these structures is often difficult if the appropriate geophysical methods are not used; consequently most boreholes drilled in the area are either unproductive or sometimes have low yield.

The existence of faults and/or fracture zones in a geologic medium contribute to enhancing the hydrogeological characteristics such as the hydraulic conductivity and secondary porosity of such a medium, while also acting as a structural control for groundwater movement. Therefore, quantifying these structures using geophysics would go a long way in assisting effective hydrogeological and engineering construction planning that may be conducted in similar environments in the future (Barker 1999 and Barker et al. 1992). It is also true that the success of borehole siting is dependent on the borehole intersecting some fracture zones in the bedrock. However, once the bedrock is covered by any thickness of weathering, the fracture zone may be difficult to find, in which case geophysics can provide an indirect solution to the problem. It is easily demonstrated that fractures of a few centimetres thickness, which may be very important hydrogeologically, cannot normally be located by geophysics once they are buried below a few metres of overburden. Research has shown that successfully sited boreholes that penetrate a fracture zone have sustainable high productivity (Medeiros and Lima 1990; Olayinka and Weller 1997; Seaton and Burbey 2002).

Some of the known geophysical methods that are commonly employed to locate fracture zones include shallow seismic reflection, seismic refraction, ground penetrating radar, borehole radar tomography, electrical

 DOI 10.1007/s10040-006-0051-2

resistivity imaging (ERI), electromagnetic, potential, and VLF methods. These techniques have become increasingly popular in pre-drilling geophysical investigations worldwide because it has been found that the use of these methods is rapid, inexpensive and helps in increasing the chances, effectiveness and efficiency of siting productive boreholes within the basement rocks. In this report, an attempt is made to offer insights into the relationship between fracture zones and overburden thickness, which can aid in siting productive boreholes in a hardrock basement area. It has been established in the past that the existence of a fracture zone in a geologic medium can greatly influence its hydrogeological characteristics (Medeiros and Lima 1990). Resistivity surveys are commonly used to map fracture zones in hard rock terrain (e.g. Barker et al. 1992, Carruthers and Smith 1992) because high resistivity contrasts usually occur between solid rocks and saturated fracture zones. The main objective of the study is therefore to detect fracture zones in the crystalline basement covered by weathered overburden having variable thickness. To achieve this aim, a synthetic numerical modelling experiment was first carried out using the DC dipole–dipole resistivity and the VLF technique to simulate the model response over the fault. The model closely approximates a geologic situation when the fault has a long strike length. The results obtained were confirmed by dipole–dipole and VLF field data acquired perpendicular to the suspected fault zone. The study site was selected based on the result of a high radon-gas anomaly identified over the fault zone by Ajayi and Adepelumi (2002). It was envisaged that low resistivity zones will indicate fracture zone location as was suggested by Apparao and Roy (1971).

Study area (Ile-Ife)

The study area shown in Fig. 1 is located at 7°26′–7°30′N latitude and 3°58′–4°30′E longitude. This region lies within the tropical rain forest of Nigeria that has two distinct seasons (wet, April–October; and dry, November–March). The annual mean rainfall is about 1,600 mm. The diurnal range in temperature is not significant, but the daily temperature can reach 29 °C and is seldom lower than 25 °C. The water table in the region is generally found at less than 12 m in depth from the ground surface.

The basement complex in the Ile-Ife area consists of two distinct lithological types—the gneisses and the schists (Fig. 1). The various rock formations found in the study area are an integral part of the basement complex rocks of Nigeria. The study area belongs to the classical schist belt of southwestern Nigeria that comprise abundant mafic rocks and a large mafic/ultramafic body that could represent remnants of an oceanic assemblage (Rahaman 1988). The area is known to have variable metamorphic mineral assemblages ranging from greenschist- to amphibolite-facies (Ajibade et al. 1987). Locally, the study area is underlain by granitic and gneissic basement rocks overlain by a relatively thick covering of weathered materials made up of a sequence of lateritic clay (aquitards), clayey sand/sand, and weathered/fractured bedrock. The shallow clay-rich aquitards serve as protection for the underlying aquifers from contamination and they assist in limiting the groundwater recharge (van der Kamp 2001). According to Acworth (1987), these are regolith materials that are normally produced by the in situ weathering of the basement rocks. The clayey sand/sand and weathered/fractured bedrock constitute the main aquifer, located within a bedrock depression that is the catchment area for the region. Groundwater occurs under water-table conditions in the clay sand/sand aquifer as well as under semi-confined to confined conditions in the weathered/fractured zone. Singh (2005) examined the correlation relationships between hydraulic permeability and transmissivity with electrical resistivity and established that there is a non-linear relationship between hydraulic conductivity (K) and apparent resistivity (ρ). This relation is given as $K = 0.0538e^{0.0072\rho}$. In this relation, ρ equals the apparent resistivity of the aquifer. The transmissivity (T)=K×h, where h is the thickness of the aquifer. The hydraulic conductivity (K) of the clayey sand/sand aquifer was estimated to vary from 1.14 to 251 m/day and the transmissivity (T) varies from 20.13 to 553.00 m^2/day. Also, the hydraulic conductivity (K) of the weathered/fractured bedrock aquifer was found to vary between 1.29 and 50.7 m/day, while the transmissivity (T) varies from 103.68 to 190.1 m^2/day. The estimated aquifer parameters suggest a moderately permeable aquifer with medium yield. Lohman (1972) suggested that storativity (S), which indicates the capability of an aquifer to store or release water as head changes, can be calculated using the known values of aquifer thickness (h) and corresponding specific storage (Ss) values given in a nomogram. Storativity (S)=Ss×h. Therefore using the empirical relation given by Lohman (1972), the storativity of the aquifers was estimated as ranging from 6.60×10^{-6} to 5.28×10^{-5} for clayey sand/sand, and 1.11×10^{-5} to 5.28×10^{-5} for weathered/fractured bedrock. Recent field evidence showed that the groundwater in the area is structurally controlled by the NE–SW trending thrust faults (F1, shown in Fig. 1), and the groundwater flows from the west towards the east and northeast (Adepelumi et al. 2001). According to Okhue and Olorunfemi (1992) subsurface ridges and depressions in the bedrock surface control the groundwater flow pattern.

Methodology employed

Direct current (DC) dipole–dipole resistivity

As a first step to this study, two-dimensional resistivity models were built using the numerical modelling program EM2DMODEL (KIGAM 2002). The information incorporated into these models was based on the available a priori geologic and geophysical information for the area obtained from recent results presented by Adepelumi et al. (2001), Okhue and Olorunfemi (1992), and Ajayi and Adepelumi (2002). The a priori information used included

 DOI 10.1007/s10040-006-0051-2

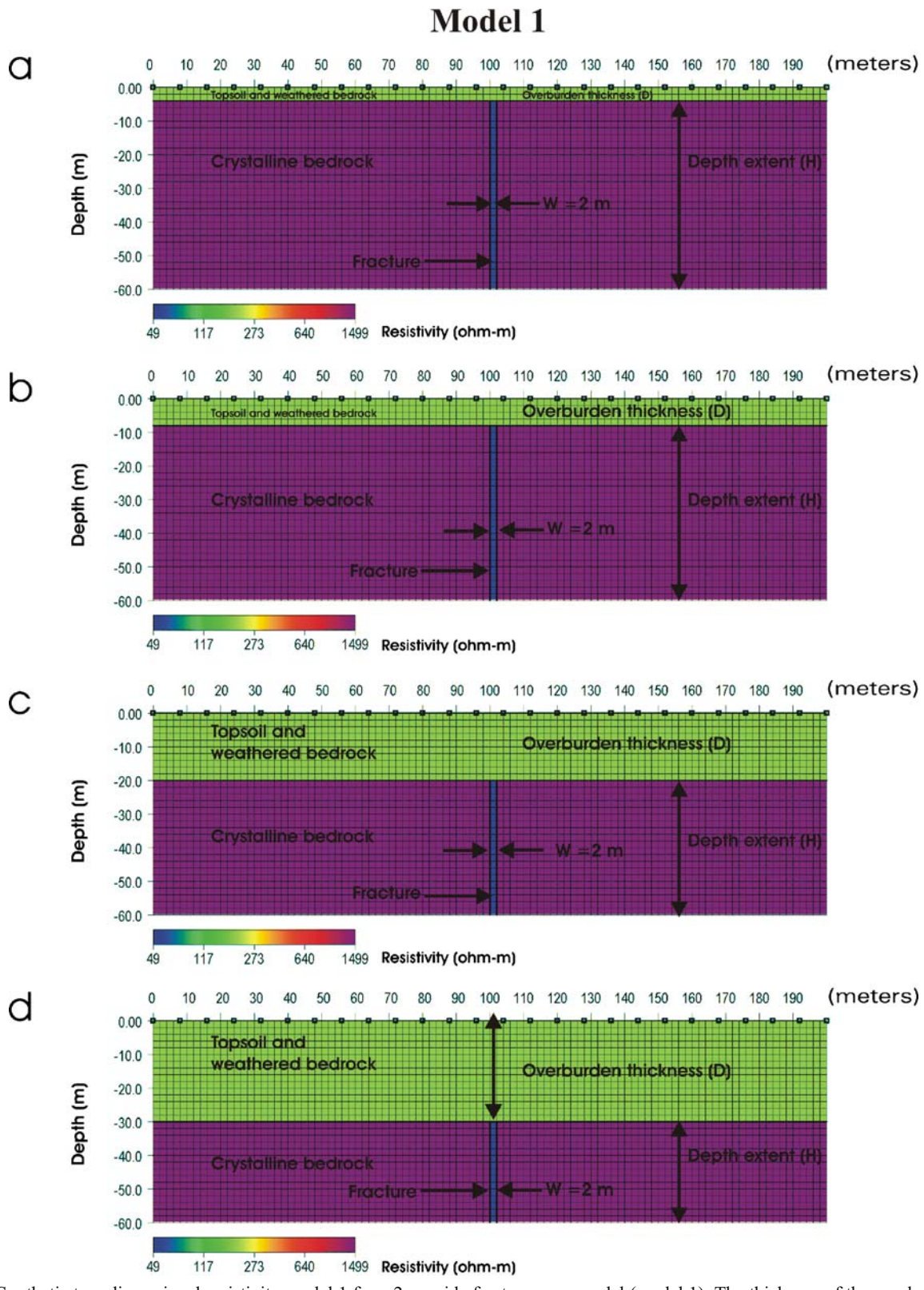

Fig. 2 Synthetic two-dimensional resistivity model 1 for a 2-m-wide fracture zone model (model 1). The thickness of the overburden was fixed at **a** 4 m, **b** 8 m, **c** 20 m and **d** 30 m

existing lithologic logs of the subsurface formation obtained from borehole drilling, and the apparent resistivity and thicknesses of the subsurface geologic sequences derived from various geophysical surveys; the a priori information was used so as to serve as a constraint for the inversion algorithm. It was thus envisaged that by using

 DOI 10.1007/s10040-006-0051-2

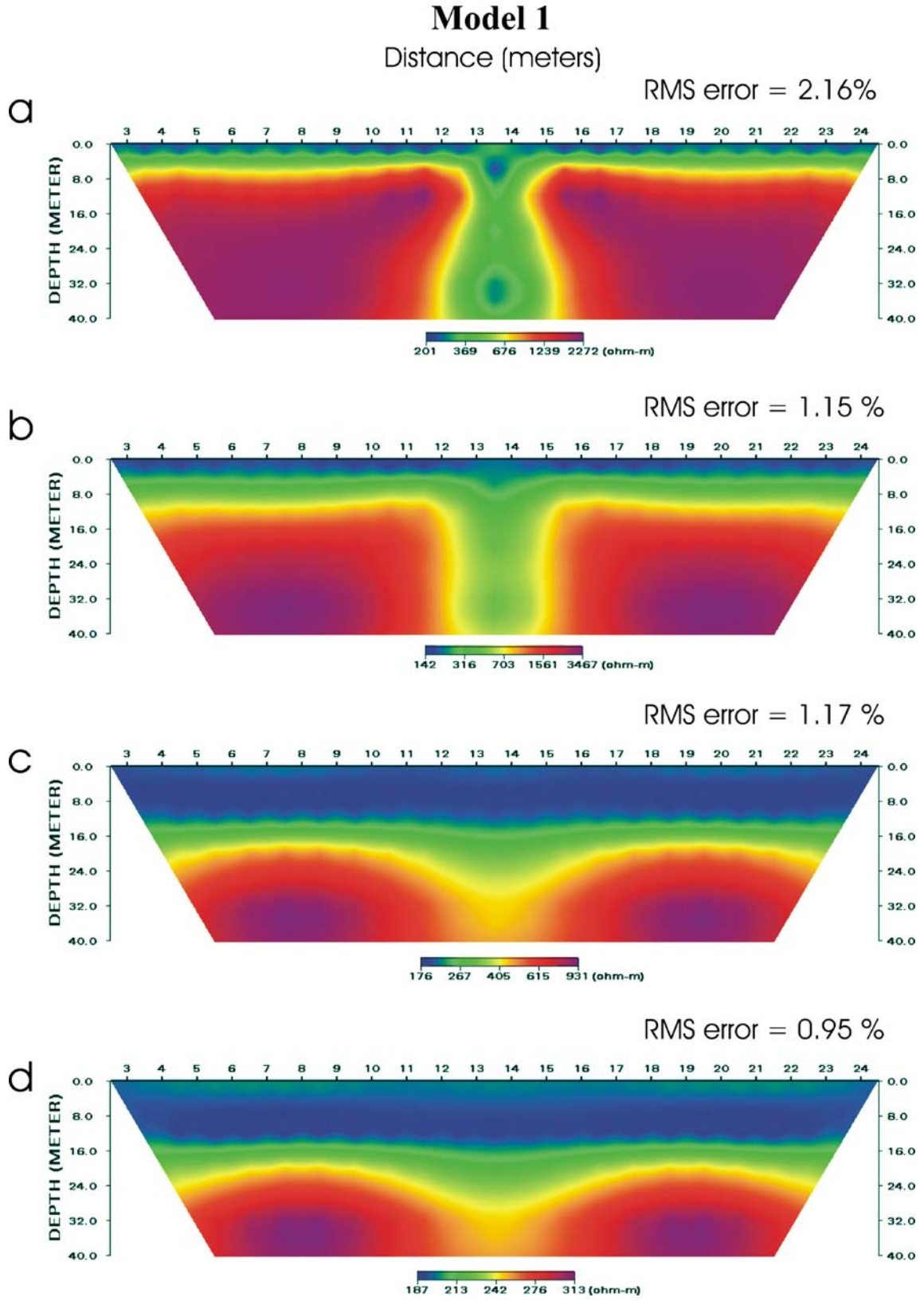

Fig. 3 Inverted resistivity pseudosections of the 2-m-single-fracture zone model obtained using the synthetic model 1 shown in Fig. 2, with overburden thickness fixed at **a** 4 m, **b** 8 m, **c** 20 m and **d** 30 m. *RMS* is root mean square

the a priori information, the subsurface resistivity image that will be obtained will be a better approximation of the subsurface geology. The synthetic resistivity models that were used represent a single fractured/faulted zone in a

 DOI 10.1007/s10040-006-0051-2

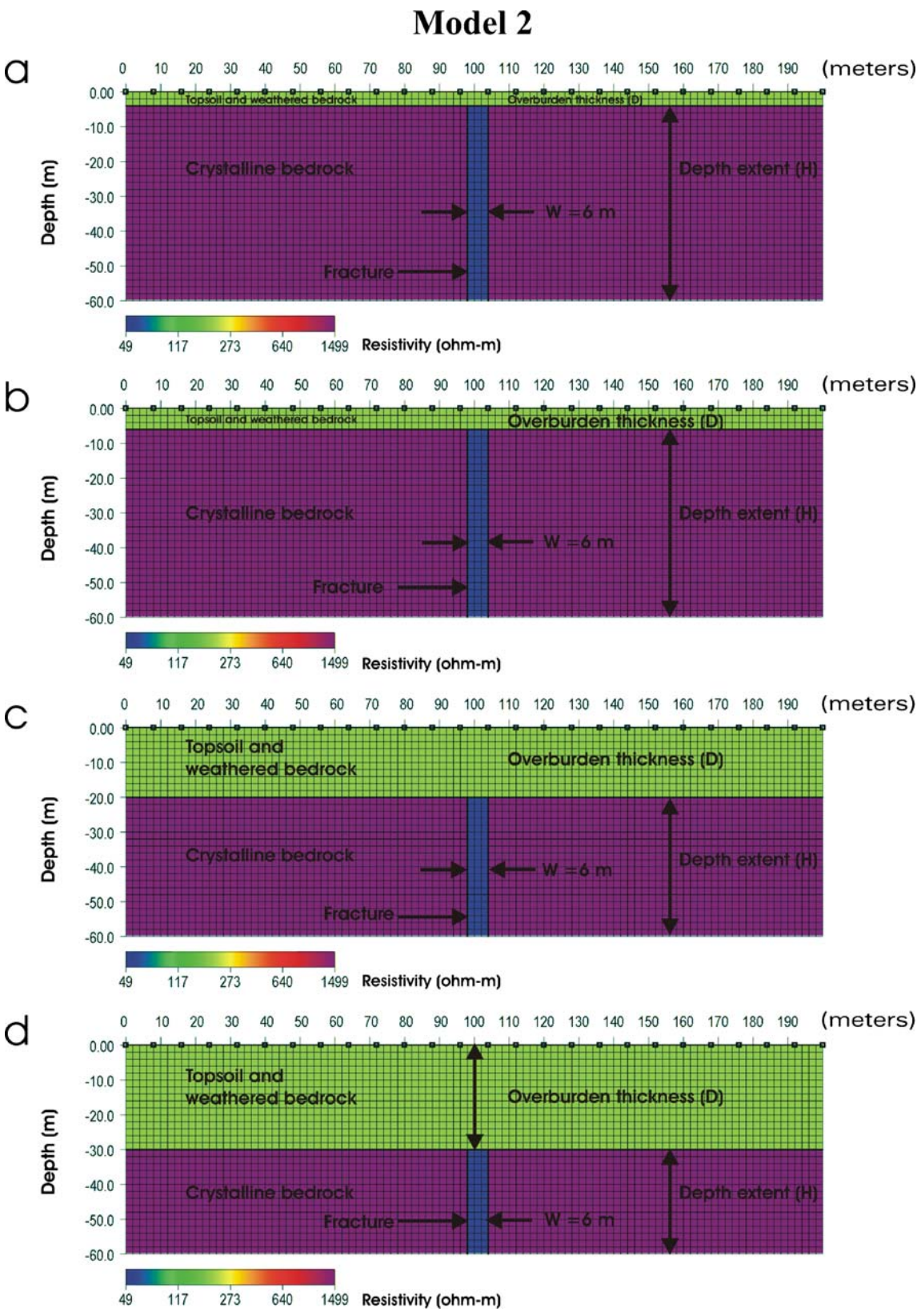

Fig. 4 Synthetic two-dimensional resistivity model 2 for a 6-m-wide fracture zone model (model 2). The thickness of the overburden was fixed at **a** 4 m, **b** 8 m, **c** 20 m and **d** 30 m

crystalline basement rock overlain by moderately resistive overburden. Using the dipole–dipole array, these models were used to generate synthetic apparent resistivity data that were later used to simulate the electrical response of

 DOI 10.1007/s10040-006-0051-2

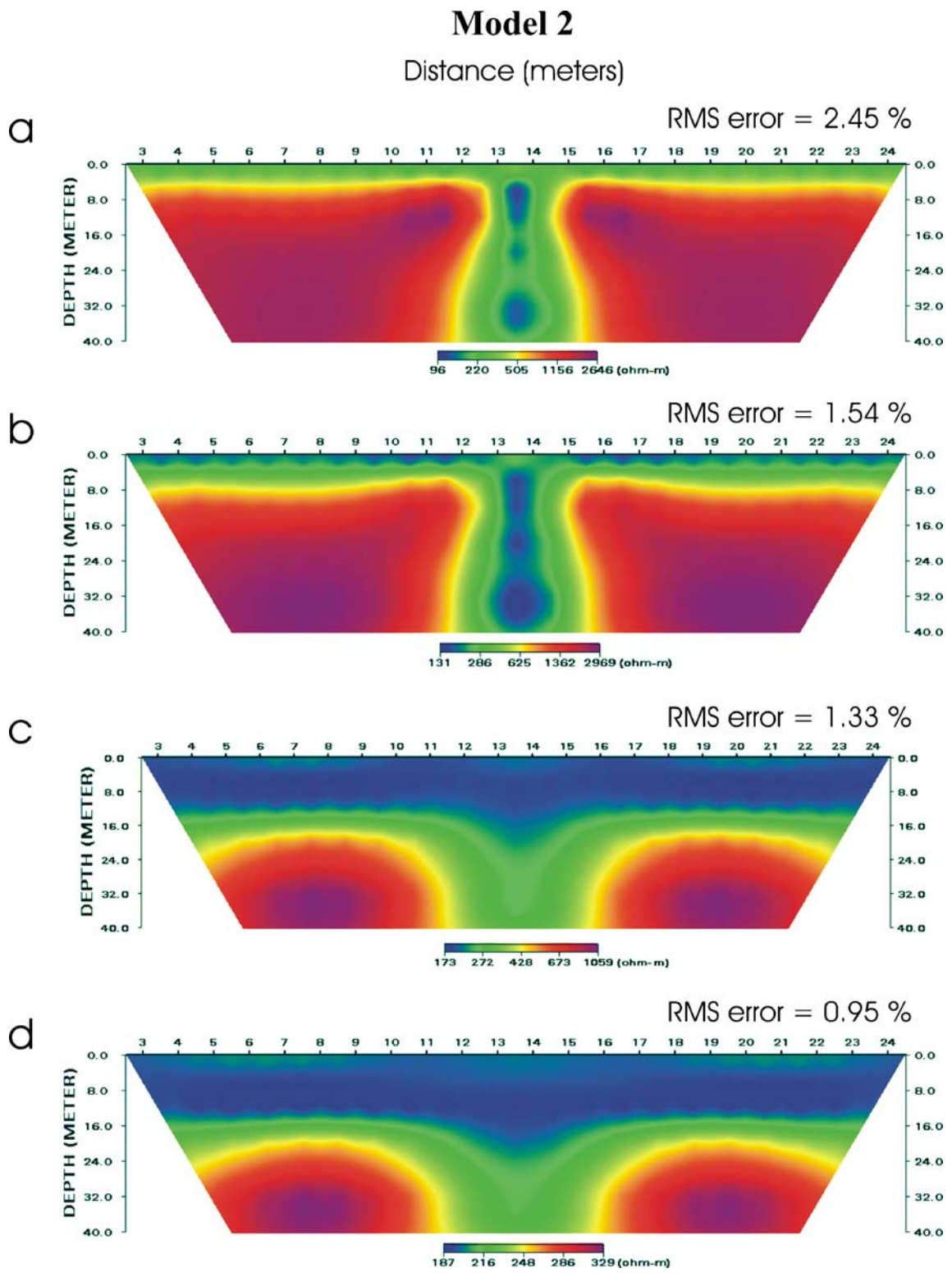

Fig. 5 Inverted resistivity pseudosections of the 6-m-single-fracture zone model obtained using the synthetic model 2 shown in Fig. 4, with overburden thickness fixed at **a** 4 m, **b** 8 m, **c** 20 m and **d** 30 m. *RMS* is root mean square

subsurface structures. By using an iterative smoothness-constrained least-squares inversion method (Yi et al. 2003), the apparent resistivity data produced from the two-dimensional forward modelling were subsequently inverted to create a model of subsurface resistivity that approximates the true subsurface resistivity distribution using DIPRO inversion program developed by the Korea Institute of Geoscience and Mineral Resources (KIGAM

 DOI 10.1007/s10040-006-0051-2

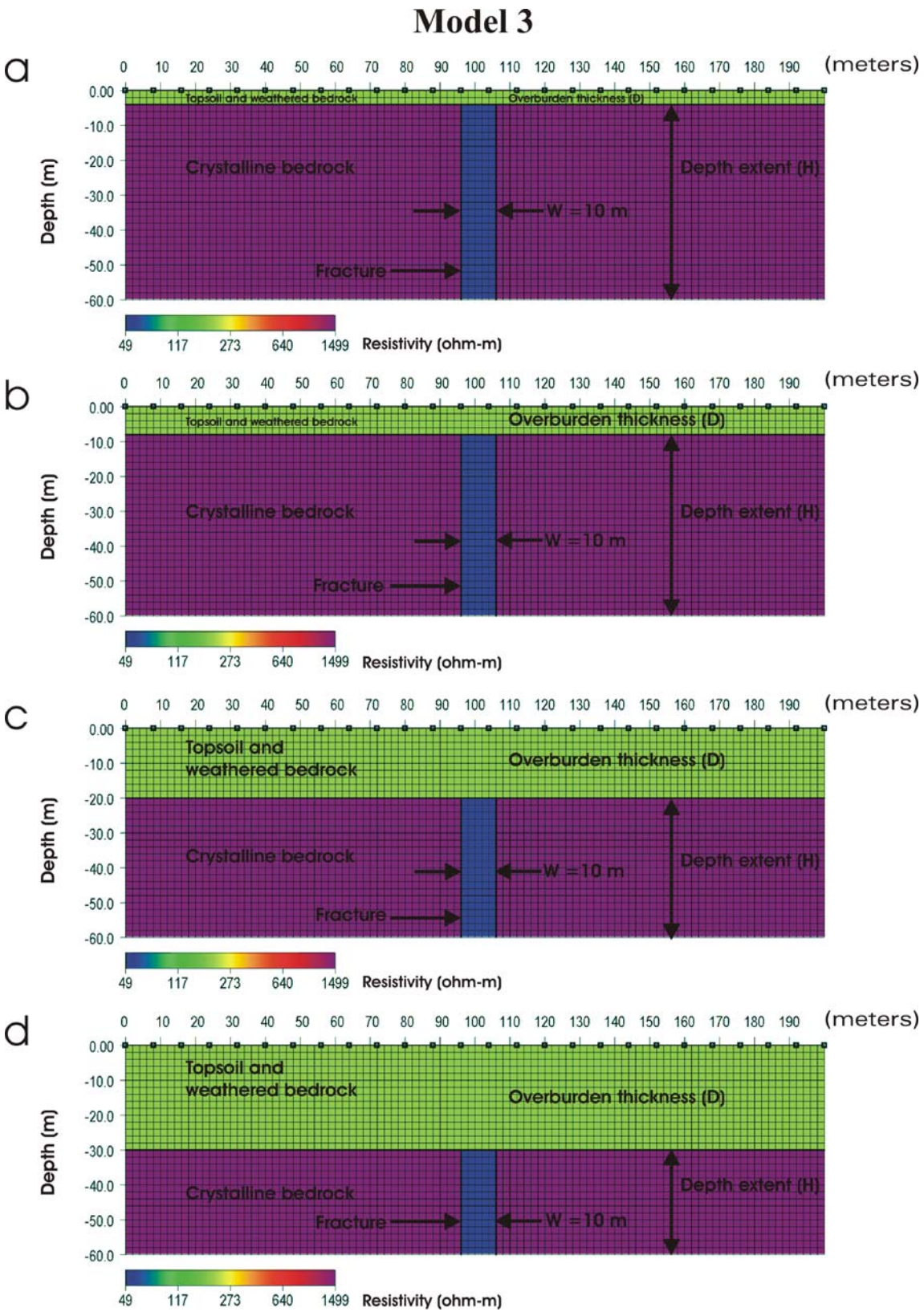

Fig. 6 Synthetic two-dimensional resistivity model 3 for a 10-m-wide fracture zone model (model 3). The thickness of the overburden was fixed at **a** 4 m, **b** 8 m, **c** 20 m and **d** 30 m

2001). The inversion programs adopted are based on the generation of a finite element method (FEM) model of the subsurface, where the model resistivities of the FEM are automatically adjusted through an iterative process so that

 DOI 10.1007/s10040-006-0051-2

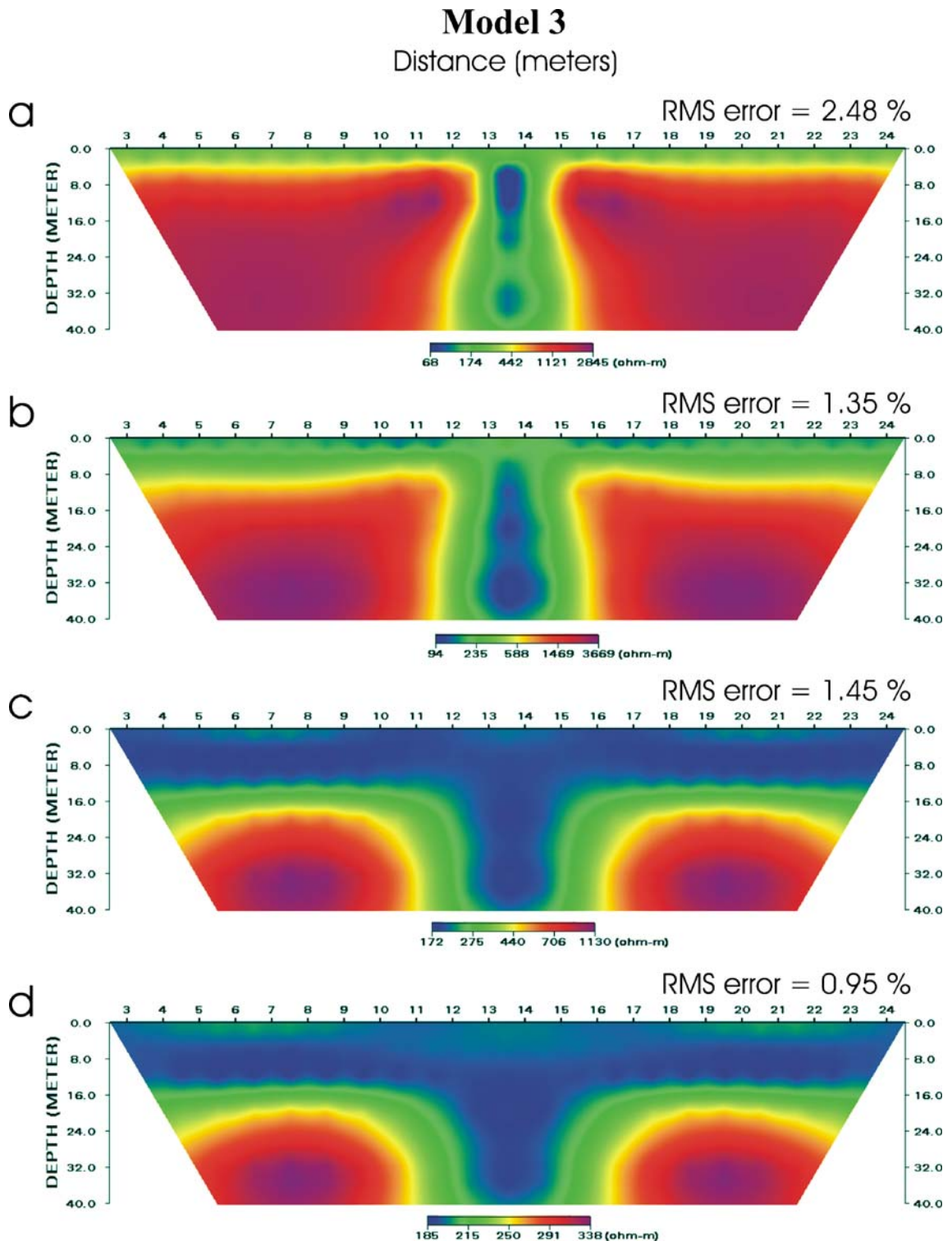

Fig. 7 Inverted resistivity pseudosections of the 10-m-single-fracture zone model obtained using the synthetic model 3 shown in Fig. 6, with overburden thickness fixed at **a** 4 m, **b** 8 m, **c** 20 m and **d** 30 m. *RMS* is root mean square

the model response converges towards the measured data. The inversion method minimizes the square of the differences between the measured and the calculated apparent resistivity values. Once this minimization is achieved, the inversion process will stop automatically as the model responses will have converged towards the measured data (Yi et al. 2003). The Marquardt approach was used for the inversion procedure, with recalculation of the Jacobian matrix after each iteration stage. During the inversion process, it was necessary to seek the appropriate subsur-

 DOI 10.1007/s10040-006-0051-2

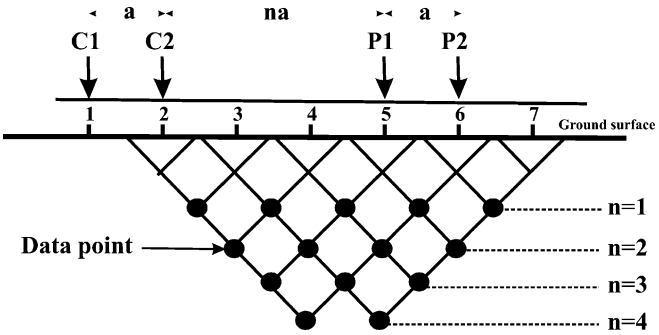

Fig. 8 Configuration of the four-electrode DC dipole–dipole array used for resistivity profiling in this study. C1 and C2 are the current electrodes; P1 and P2 are the potential electrodes, while *a* is the spacing between electrodes used for each measurement and *n* is the expansion factor (integer values 1–6). The separation between dipoles is always a multiple (*n*) of *a*. Numbers *1–7* are the electrode (current and potential) station positions in metres

face resistivity model that represented a compromise between the data fit and model smoothness. An optimum smoothness was therefore found based on the misfit minimization at each iteration step. The Lagrange multiplier (λ) or damping factor incorporated in the smoothness–constraint inversion program was used as a weighting factor to control the inversion scheme. This weighting factor serves as a stabilizer during each iteration step of the inversion process, and it also helps in improving the resolution of the image obtained. In other words, λ can be viewed as a sensitivity parameter, which essentially controls the root mean square (RMS) value between the data and the model. The optimum λ values were obtained on a trial-and-error basis by first choosing a minimum value of 0.001 and increasing by one order in each of the successive iterations. A λ value of 0.01 was found to be appropriate for the field data set. In this case, for values of λ above and below 0.01, the data fit degraded, resulting in rougher models, hence the choice of λ=0.01. For the two-dimensional inversion, ten iterations were implemented, since after ten iterations it was observed that the model residuals do not change much and the inversion algorithm had converged to constant RMS levels of 1.82% for profile A-A′ and 3.99% for profile B-B′. Topography data were also incorporated into the resistivity models so that topographic effects could be accounted for because these effects are very significant in the study area.

Three different fracture zone models were considered in this study. Figures 2 and 3 show the synthetic two-dimensional resistivity model of a 2-m-wide fracture zone and the corresponding inverted resistivity pseudosection for model 1. Likewise, the synthetic two-dimensional resistivity model of a 6-m-wide fracture zone and the equivalent inverted resistivity pseudosection for model 2 is shown as Figs. 4 and 5. For model 3, the synthetic two-dimensional resistivity model of a 10-m-wide fracture zone and the retrieved inverted resistivity pseudosection for the model is shown as Figs. 6 and 7. In these three models, a resistivity value of 50 ohm-m was assigned to the fracture zone. The resistivity of the top layer (overburden) was represented by 200 ohm-m. According to Olayinka and Weller (1997), the assigned resistivity of the overburden should be the weighted average of the various geoelectrical units that make up the overburden in a crystalline basement terrain which is lumped together and shown as having a single resistivity as shown in the models. A resistivity of 1,500 ohm-m was assigned to the granitic and/or gneissic basement host rocks. A 2% Gaussian noise representing instrumental noise was added to the synthetic data so as to simulate field conditions. For each model, numerical modelling and inversion was carried out for four cases of overburden thicknesses, i.e. 4, 8, 20 and 30 m. These overburden thicknesses represent a typical scenario in the hard rock terrain of Ile-Ife. The effect of increasing the overburden thickness and width of the fracture zone on the resulting resistivity images derived from the inversion were studied.

A Terrameter (SAS 300C, ABEM, Sweden) was used for the data acquisition in profiling mode using the dipole–dipole array with electrode spacing of 10 m (Fig. 8). The *n* is the expansion factor of the dipole–dipole array that controls the depth of investigation. This factor represents the ratio of the distance between the current (C1) and potential (P1) electrodes to the C2-C1 (current dipoles) or P1-P2 (potential dipoles) separation "*a*". The spacing between the current electrode pair C1-C2 and P1-P2 is given as *a*. The *n* values of the array were varied from 1 to 6 during the field survey. The two survey lines were 200 m long each, and were set-up in an NW–SE orientation across the suspected main fault (profiles A-A′ and B-B′ in Fig. 1). Dipole–dipole resistivity surveys were performed along the lines. Dipole–dipole resistivity surveying is a geophysical technique consisting of four electrodes distributed in a collinear array, as shown in Fig. 8. This method provides information pertaining to both the depth and lateral extent of electrical resistivity variations. The survey is usually conducted by introducing current into the subsurface with a current dipole (C1 and C2) and measuring the resulting ground voltage along a survey line using a potential dipole (P1 and P2). Subsurface features are imaged based on contrasts in resistivity (Figs. 3, 5 and 7). Both pairs of electrodes (C1–C2 and P1–P2) are referred to as dipoles, and both dipoles have the same length (*a*). The separation between dipoles is always a multiple (*n*) of *a*. Depth of investigation

 DOI 10.1007/s10040-006-0051-2

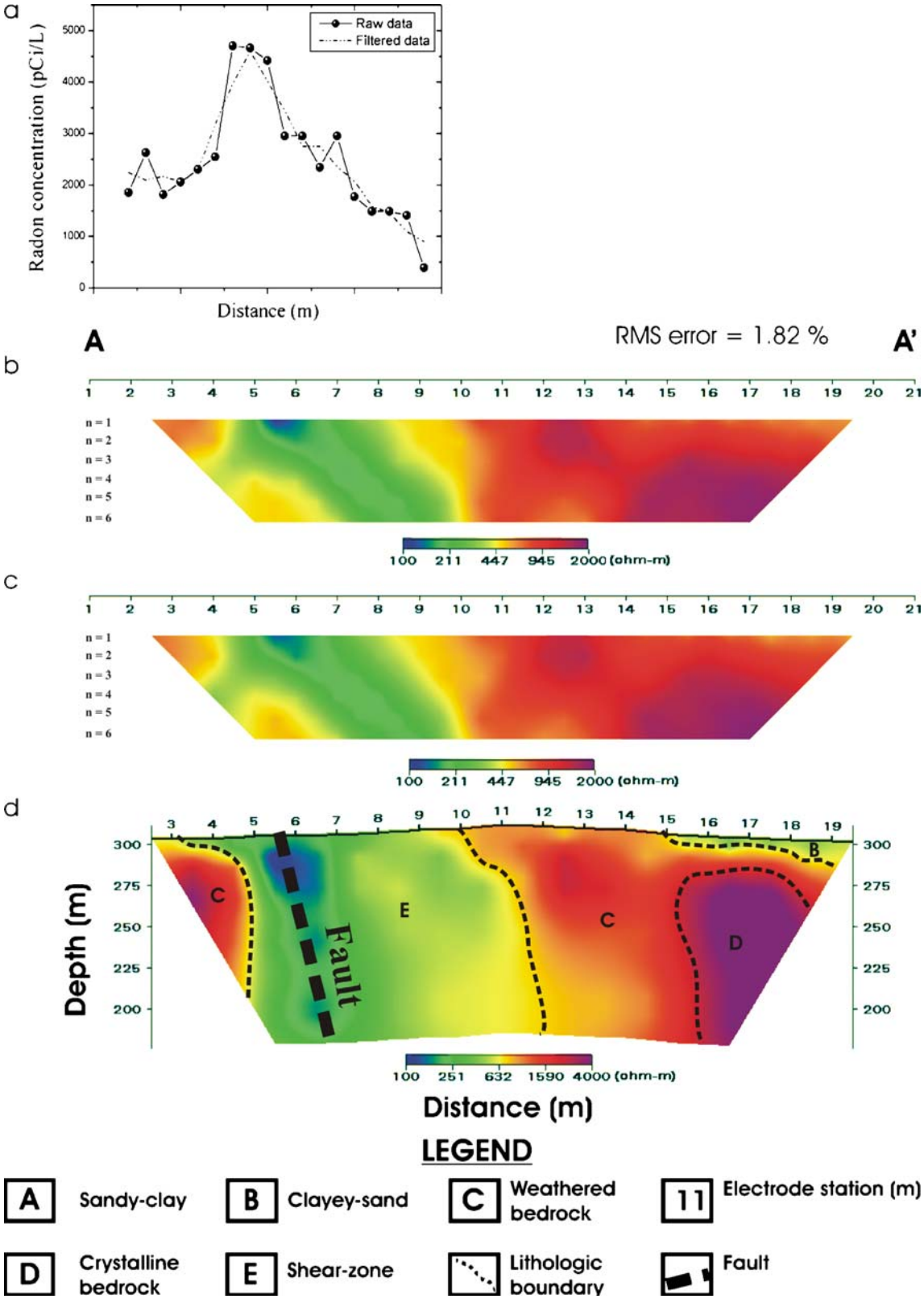

Fig. 9 **a** Radon anomaly and **b**–**d** geoelectrical models of profile A-A′. The model was obtained by inverting the acquired field DC dipole–dipole resistivity data shown in **b**. The theoretically computed data is shown in **c**. The model shown in **d** converges at 1.82% *RMS* error. Topography effects were incorporated into the inversion process. Numbers *1–20* along the top are the electrode (current and potential) station positions in metres

increases with increase in distance between the dipoles. It has been shown that dipole–dipole array has greater depth of penetration compared to other resistivity methods (Seaton and Burbey 2002). In order to ascertain the

 DOI 10.1007/s10040-006-0051-2

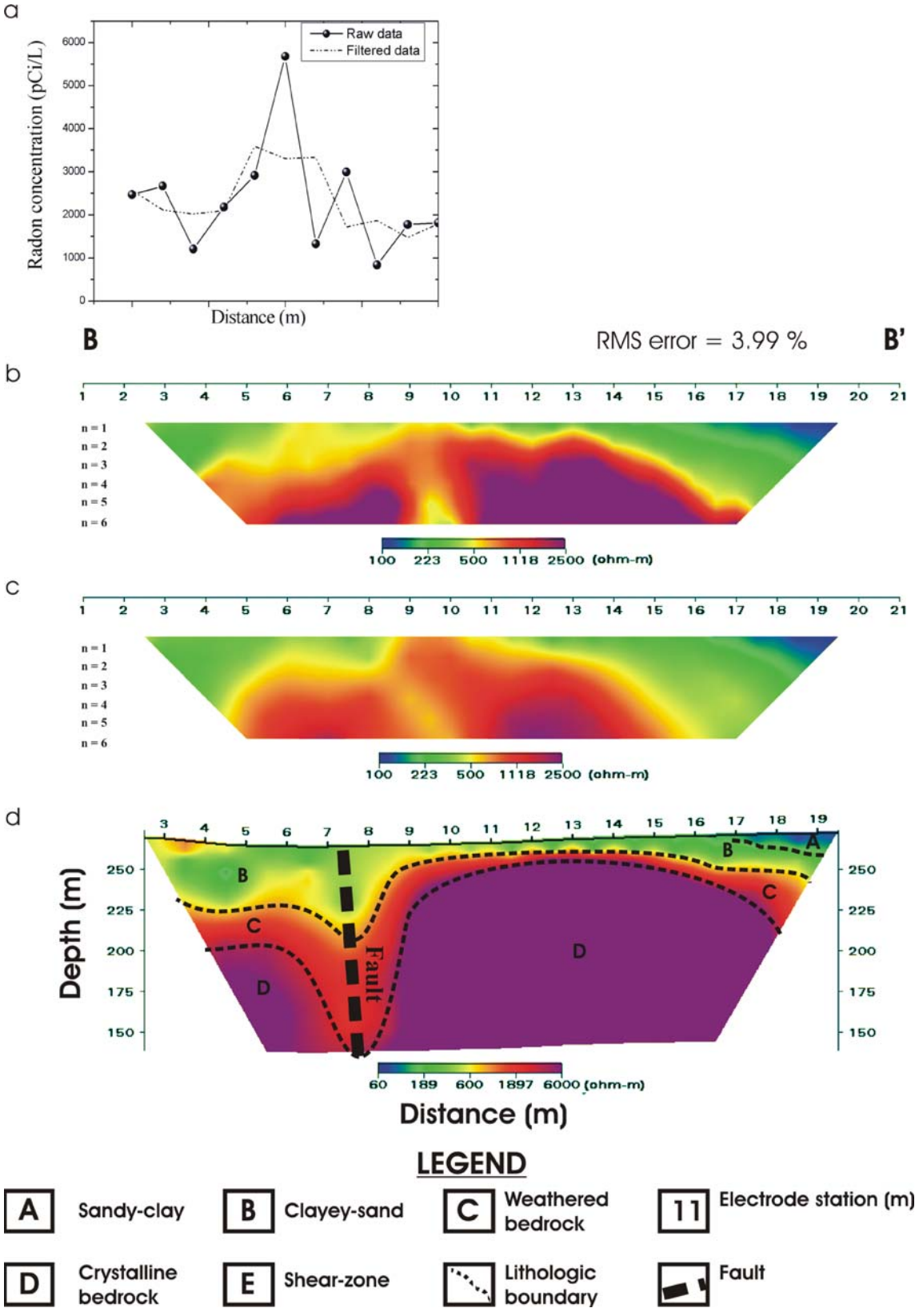

Fig. 10 **a** Radon anomaly and **b**–**d** geoelectrical models of profile B-B′. The model was obtained by inverting the acquired field DC dipole–dipole resistivity data shown in **b**. The theoretically computed data is shown in **c**. The model shown in **d** converges at 3.99% *RMS* error. Topography effects were incorporated into the inversion process. Numbers *1–20* along the top are the electrode (current and potential) station positions in metres

 DOI 10.1007/s10040-006-0051-2

quality and consistency of the field measured data, and also to detect and remove erroneous data, four resistivity measurements were taken at each measurement point and then compared with each other. A resistivity value that was found to be within 2% of the previous measurement taken at the same point was accepted as a valid measurement. On the other hand, measurements with greater than 2% error were rerun with higher current so as to lower the percentage difference between the compared values.

Very low frequency electromagnetics (VLF)

The VLF method is an inductive exploration technique that is used primarily to map shallow subsurface structural features in which the primary electromagnetic (EM) wave induces current flow (Sinha 1990, Kaikkonen and Sharma 1997). In principle, it utilizes transmitters operating between 15–30 kilohertz (kHz) as the primary EM wave source. The EM waves propagating into the ground from the source (H_p) induce electric current in any subsurface conductor in their path. The induced current produces a secondary electromagnetic field (H_s). The vector sum of the primary field (H_p) and secondary field (H_s) produces the elliptically polarized field over time. This elliptically polarized field consists of two components of the same frequency but of different amplitudes and out-of-phase with each other. The amplitude of the component which is in-phase with the primary field (H_p) is the tilt angle, while the component which is out-of-phase with the primary field is the ellipticity. The inclination of the major axis of the polarization ellipse from the horizontal is known as the tilt angle (θ). Ellipticity (e) is the ratio of the minor axis to the major axis of the polarization ellipse of the EM fields.

The VLF transmitting stations are located worldwide. The VLF station (GBR) situated in Rugby, UK was selected for the survey because it is the only detectable VLF signal at the survey site in Nigeria. The GBR station transmits a VLF signal at a frequency of 16.0 kHz. The line of primary magnetic field emanating from the station is approximately perpendicular to the regional geologic strike of the study area which makes it ideal for the survey. VLF from both the NAA (VLF transmitter station located in Cutler, USA transmitting at a frequency of 24.0 kHz) and FUO (VLF transmitter station located in Bordeaux, France transmitting at a frequency of 15.1 kHz) could not be detected, even though Palacky et al. (1981) detected them in Burkina Faso. Far from the transmitter, the VLF signal over a uniform or horizontally layered earth consists of a vertical electric field component and a horizontal magnetic field component, each perpendicular to the direction of propagation (McNeill 1990, and Sinha 1990). Because the source of the electromagnetic field originates from a remote distance, the long wavelength EM wave approximates a plane wave.

Simple geologic models were built that closely match the field conditions found in the study area. Thereafter, numerical VLF modelling was conducted to simulate these geologic conditions using the multi-purpose program EM2DMODEL, which was developed by KIGAM (2002) to numerically model both the electrical and electromagnetic synthetic data. In this study, the initial models 1, 2 and 3 shown in Figs. 2, 4 and 6 were used as the input for the VLF modelling exercise because the results from the dipole–dipole field data were in general agreement with the numerical modelling experiments. The models were therefore assumed to closely approximate the subsurface electric structure beneath the survey lines. Having in mind the success of the dipole–dipole modelling result, calculations were then undertaken for both the in-phase (tilt angle) and out-of-phase (ellipticity) components of the induced electromagnetic field of the VLF models assumed. McNeill and Labson (1991) showed that the induced current flowing in fracture zones usually produces a secondary magnetic field that is out-of-phase with the primary magnetic field which would aid in the easy detection of fractures zone. Both the tilt-angle (θ) and ellipticity (e) of polarization ellipse of the EM fields were computed using the formulae proposed by Smith and Ward (1974), which are expressed as:

$$\tan 2\theta = \pm \frac{2(H_z/H_x)\cos\Delta\phi,}{1-(H_z/H_x)^2} \tag{1}$$

$$e = \frac{H_z H_x \sin\Delta\phi}{H_1^2}, \tag{2}$$

where H_z and H_x are the amplitudes, the phase difference $\Delta\phi=\phi_z-\phi_x$, in which ϕ_z is the phase of H_z and ϕ_x is the phase of H_x and $H_1 = \left|H_z e^{i\Delta\phi}\sin\theta + H_x\cos\theta\right|$. A qualitative method was used to interpret the VLF tilt-angle data to identify fracture zones by comparing the computed data to the measured and modelled dipole–dipole resistivity results shown in Figs. 2, 3, 4, 5, 6, 7, 9 and 10. According to Saydam (1981), the top of the fracture zone will be centred at the inflection point of the tilt-angle and ellipticity anomaly response. During this study, responses over the vertical fracture zones were computed at a fixed frequency of 16 kHz. Therefore the computed results are assumed to be representative of field data acquired at that frequency in a similar hard-rock terrain having similar geology as the study area.

The apparent resistivity ρ_a (ohm-m) and phase angle φ (^{o}) of the synthetic model over the suspected fault were calculated using the relation given by Kaikkonen (1980) as:

$$\rho_a = \frac{1}{\omega\mu}\left|\frac{E_{y,x}}{H_{x,y}}\right|^2, \tag{3}$$

$$\varphi = \arctan\left[\frac{\mathrm{Im}\left(E_{y,x}/H_{x,y}\right)}{\mathrm{Re}\left(E_{y,x}/H_{x,y}\right)}\right], \tag{4}$$

 DOI 10.1007/s10040-006-0051-2

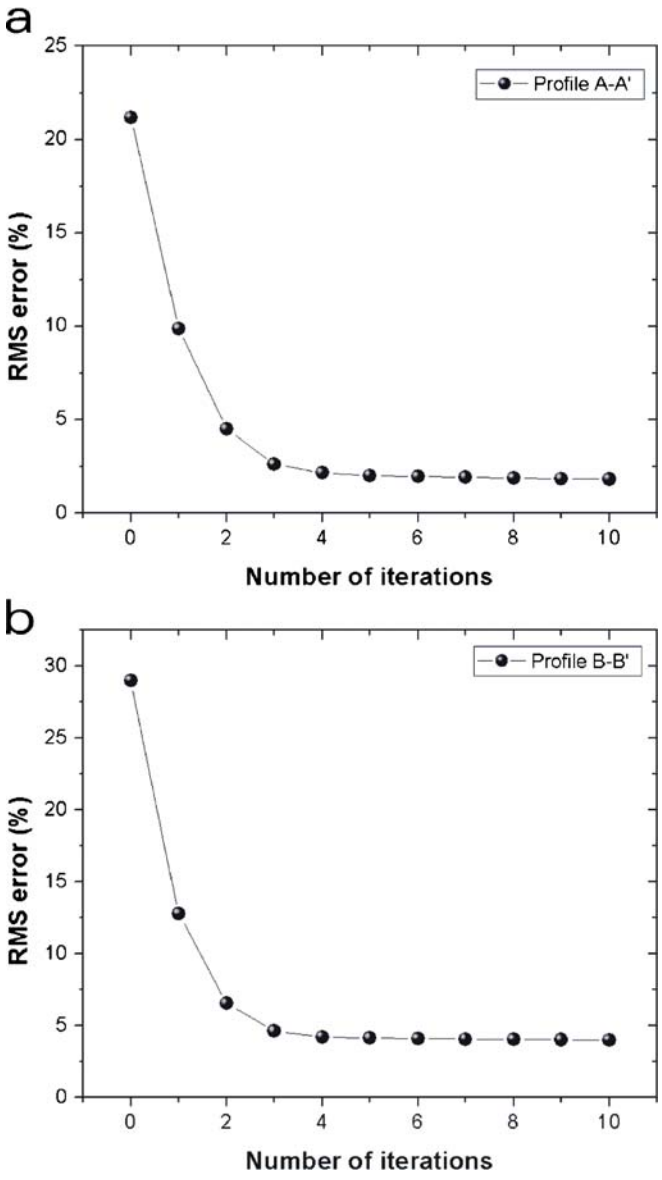

Fig. 11 Root mean square (*RMS*) error curves for the two-dimensional inversion of field data, showing errors for **a** profile A-A′ and **b** profile B-B′

where ω is the angular frequency of the VLF primary field and μ is the magnetic permeability of the subsurface. E_x and E_y are the orthogonal horizontal electric field. H_x and H_y are the orthogonal component of the magnetic field. Also, low resistivity zones were interpreted as possible fracture zones in the computed VLF-R resistivity data.

Results and discussion

Theoretical dipole–dipole data

The synthetic resistivity vertical fault models and their inversion results are shown in Figs. 2, 3, 4, 5, 6, 7, 9 and 10. Inversion of the theoretical resistivity data indicate that the estimated resistivity of the fracture zone is approximately 137 ohm-m (model 1), 76 ohm-m (model 2) and 62 ohm-m, whereas the maximum resistivity of the surrounding host rock is approximately 4,700 ohm-m (model 1), 4,800 ohm-m (model 2) and 4,845 ohm-m (model 3). In general, resistivity of the host rock decreases as the overburden thickness increases. In all the theoretical models, the overburden is estimated to have a resistivity varying from 166 to 650 ohm-m (model 1), 100 to 600 ohm-m (model 2) and 190 to 370 ohm-m (model 3). The most important information obtained from the theoretical model result is that small fracture zone size (w) does not have any effect in the resulting inverted resistivity images. However, the fracture zone size begins to influence the model response as its size reaches half the overburden thickness (D), or more as the case may be. This result suggests that a large fracture zone size would lead to distinct model response that would depict the

 DOI 10.1007/s10040-006-0051-2

anomaly zone very clearly. For example, in models 1 and 2, it could be seen that as the thickness of the overburden increases, the inverted model loses resolution of the fracture zone (Figs. 3 and 5). However, the same effect is not so distinct in model 3 (Fig. 7). This is probably due to the decrease in the ratio between the overburden thickness (D) and the fracture zone size (w), whereas in models 1 and 2, this ratio is very large. Furthermore, a distinct depression of the basement topography characterizes the centre of the models. The origin of this depression is attributed to fracturing of the bedrock which resulted in increase in the thickness of the overburden in that zone. In general, a prominent low resistivity zone corresponding to the location of the fracture zone is clearly delineated at the centre of all the synthetic models. In addition, the geometry and absolute value of this low resistivity anomaly zone is well reconstructed and recovered after the inversion. According to Olayinka and Barker (1990), such low resistivity anomaly zones in the basement complex of Nigeria are known to be favourable to groundwater accumulations since their hydrogeological characteristics such as the hydraulic conductivity and porosity have been enhanced. As a result, any borehole drilled at that location is expected to have high yield that will have long sustainability. Also, in the theoretical model results, the host rock resistivity is well recovered and the retrieved resistivity values of the basement match quite well with the host rock resistivity obtained by Adepelumi et al. (2001), and Okhue and Olorunfemi (1992). It is evident that overburden thickness (D) and the fracture zone size (w) played a prominent role in the overall model responses that were obtained. Also, in a basement terrain, areas having thick overburden and a low resistivity zone associated with basement depression are a direct indicator of the existence of possible fractures or network of fractures having secondary porosity that will be favourable to groundwater accumulations.

Dipole–dipole field data

Figures 9b and 10b show the observed apparent resistivity data plotted as a conventional pseudosection, with apparent resistivity plotted against pseudo-depth for profiles A-A′ and B-B′, respectively. These data have been inverted to produce the images of Figs. 9d and 10d. Figure 10d clearly shows high resistivity bedrock overlain by low resistivity weathered material. The bedrock topography is variable along the two profile lines with overburden thickness varying between 5 and 40 m. Depth to the bedrock is deeper along profile B-B′ than along line A-A′.

The geoelectrical model of profile A-A′ is presented as Fig. 9d with an RMS error of 1.82%. There is a large drop in the RMS error within the first five iterations. At the end of the tenth iteration, the RMS error had converged to 1.82 from 21.17% (Fig. 11a). The final geoelectrical model shown in Fig. 9d was obtained at this stage. In this model, areas having resistivity values ranging between 2,000 and 4,000 ohm-m (high resistivity) were interpreted as crystalline bedrock (D). Areas having resistivity values ranging from 700 to 1,999 ohm-m (moderate resistivity) were interpreted as weathered bedrock (C). Zones having resistivity ranging between from 400 to 599 ohm-m (low resistivity) were interpreted as clayey-sand soil (B). Zones having resistivity values in the range of 250–399 ohm-m (very low resistivity) were interpreted as sandy-clayey-sand/top soil (A). Units A and B constitute the overburden in this study area. Finally, areas where resistivity was less than 250 ohm-m were interpreted as representing the fractured/shear zone or highly fractured rock saturated with water. From the pseudosection of this profile, a broad low resistivity anomaly is detected between electrodes 4 and 7. This anomaly is subvertical and extends to a considerable depth along this profile. Its location corresponds to the high radon anomaly earlier delineated by Ajayi and Adepelumi (2002). There is also a sharp resistivity contrast associated with this anomaly and the host rock.

Figure 10d shows the inverted two-dimensional resistivity results for lines B-B′ with an RMS error of 3.99% obtained at the tenth iteration which converged from 29.01% at the first iteration. The same error tendency of a large drop in the RMS error within the first five iterations and a slight drop after the fifth iteration was observed in this model as that of Fig. 11. At the end of the tenth iteration, the RMS error had converged to 3.99% (Fig. 11b). The final geoelectrical model shown in Fig. 10d was obtained at this stage. In this model, areas of high resistivity (≥2,000 ohm-m) were interpreted as crystalline bedrock (D). Areas of moderate resistivity (≥1,000 ohm-m) were interpreted as weathered bedrock (C). Zones with low resistivity (≤400 ohm-m) were interpreted as clayey/sand soil (B). Zones with very lower resistivity (≤200 ohm-m) were interpreted as sandy-clay/top soil (A). Areas where resistivity was less than 200 ohm-m coupled with basement depression was interpreted as representing a fractured zone having secondary porosity due to the fracture formation.

In general, in the three models, one distinct well-defined anomalous zone predominantly trending in a NE–SW direction was detected along the two profile lines A-A′ and B-B′. This anomaly transects the two lines. The trend of this anomaly coincides with the trend of the suspected fault within the basement in the study earlier delineated by Ajayi and Adepelumi (2002). Figures 9a and 10a show the location of the radon anomaly observed by the authors that is plotted on the inversion results. The only plausible explanation for the existence of this low resistivity anomaly is the presence of fracture/fault in this zone. The characteristic of this anomalous zone varies from profile A-A′ to profile B-B′. The fracture zone is located from 4 to 7 m on line A-A′ (Fig. 9d) and from 5 to 8 m on line B-B′ (Fig. 10d). The strike of this fracture zone across line A-A′ and profile B-B′ is approximately north 30 degrees east. The inverted resistivity image suggests the fracture zone is regular, indicating that a fracture zone may be producing the observed anomaly. The fracture zone consists of highly fractured and incompetent bed-

 DOI 10.1007/s10040-006-0051-2

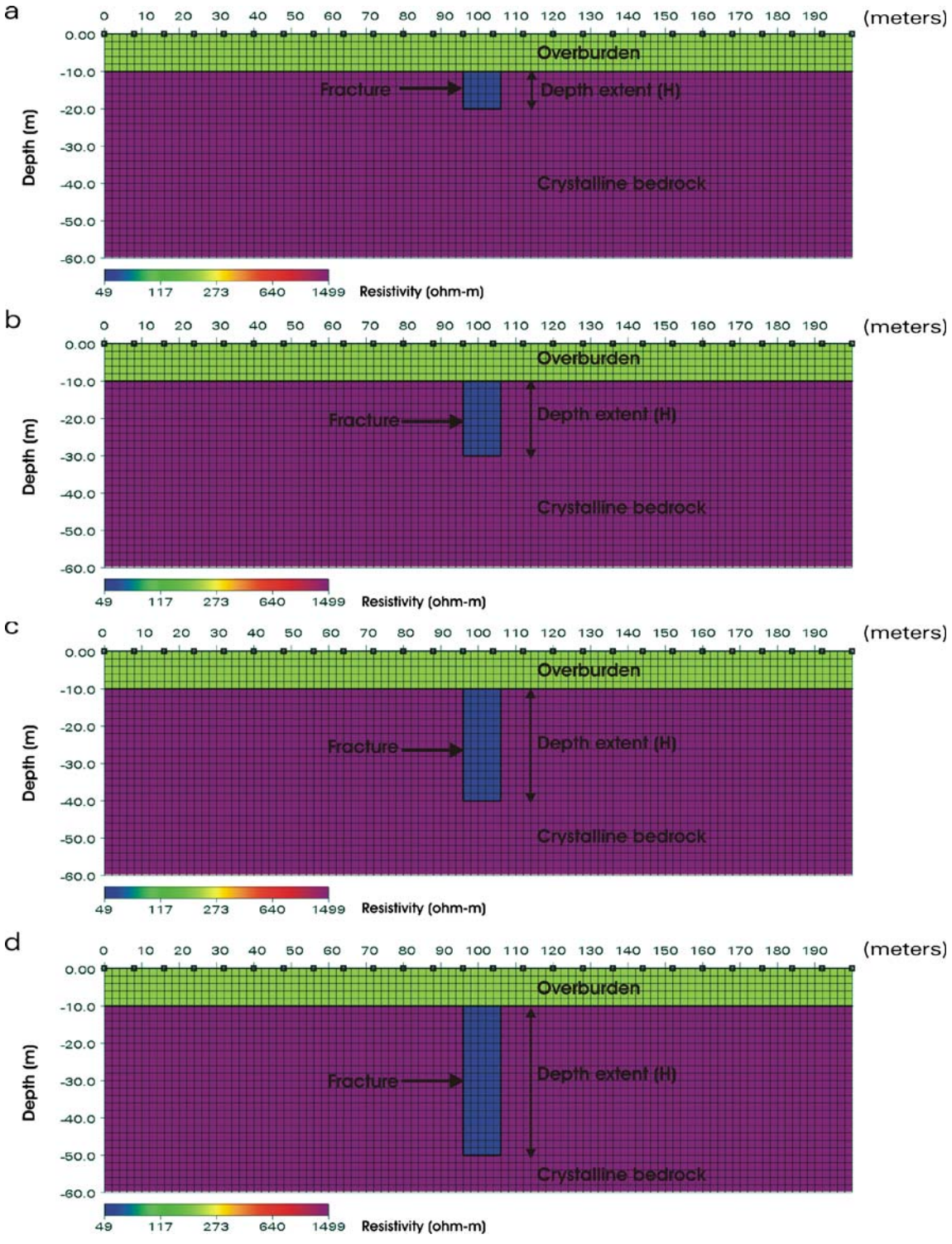

Fig. 12 A synthetic two-dimensional resistivity model for a 10-m-wide fracture zone of fixed overburden thickness (10 m). The depth extent of the fracture zone was fixed at **a** 10 m, **b** 20 m, **c** 30 m and **d** 40 m

rock. On the two profiles, the anomaly that characterizes the fracture zone is subvertical, suggesting that the fracture zone extends to the two lines. A comparison of profile A-A′ with B-B′ shows that the fracture zone seems more developed along profile A-A′ than B-B′. This suggests that the overburden is thinner along profile A-A′ and thicker along profile B-B′. This observation confirms the results of the modelling shown in Figs. 2, 3, 4, 5, 6, 7, which shows that fracture zones become less distinct as the overburden gets thicker. Inversion of the field data indicates that the fracture zone has an average resistivity value of 100 ohm-m in line A-A′ and 400 ohm-m in line B-B′.

In addition, the observed low resistivity zone within the basement along the two lines probably suggests water

 DOI 10.1007/s10040-006-0051-2

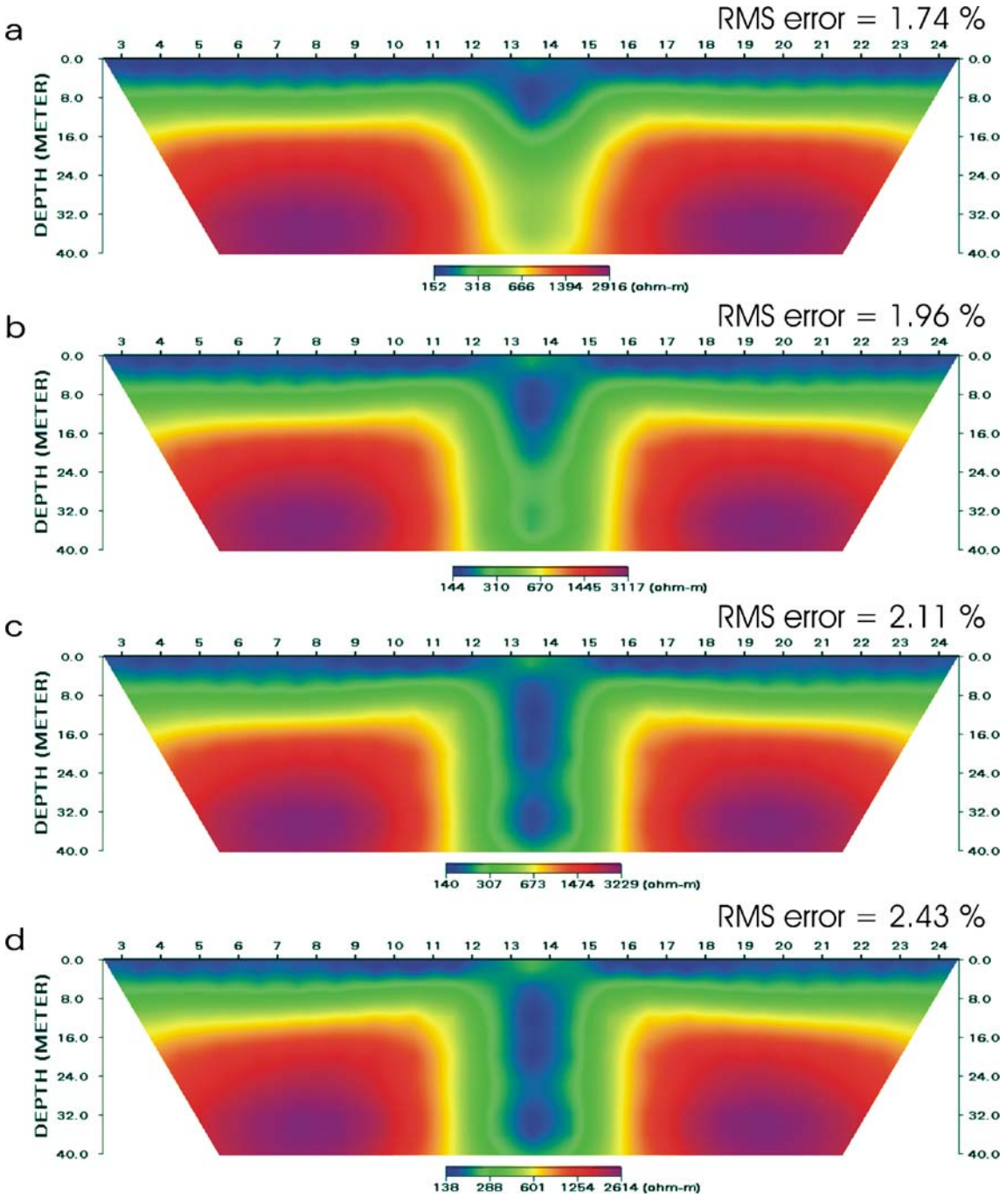

Fig. 13 Inverted resistivity pseudosection of the 10-m-single-fracture zone of fixed overburden thickness (10 m) obtained using the synthetic two-dimensional model shown in Fig. 12, with depth extent of the fracture zone fixed at **a** 10 m, **b** 20 m, **c** 30 m and **d** 40 m

saturation in the zone, which indicates that porosity is very high and, thus, that the basement rock is actually fractured with water circulation taking place within this zone. Thus in the two sections (Figs. 9d and 10d), the low resistivity zones are interpreted as fractured basement saturated with water. The resistivity of the fractured zone is lower along profile A-A′ than at line B-B′. The possible explanation for this is the higher level of fracturing at profile A-A′ (Fig. 9d), with a higher content of water.

A comparison of the synthetic inverted resistivity images (Figs. 2, 3, 4, 5, 6, 7) with the inverted field resistivity images (Figs. 9d and 10d) shows that the images of the subsurface beneath profile A-A′ and B-B′ were well reconstructed and the resistivity values recovered approximates the actual situation. Furthermore, based on the low resistivity observed in the pseudo-sections between electrode stations 4 and 7 on line A-A′ (Fig. 9d) and electrode stations 5–8 on line B-B′ (Fig. 10d), the delineated fractured zone along these lines is suspected to have developed secondary porosity which normally accompany a fracturing process within the basement, thus acting as structural control for groundwater movement.

 DOI 10.1007/s10040-006-0051-2

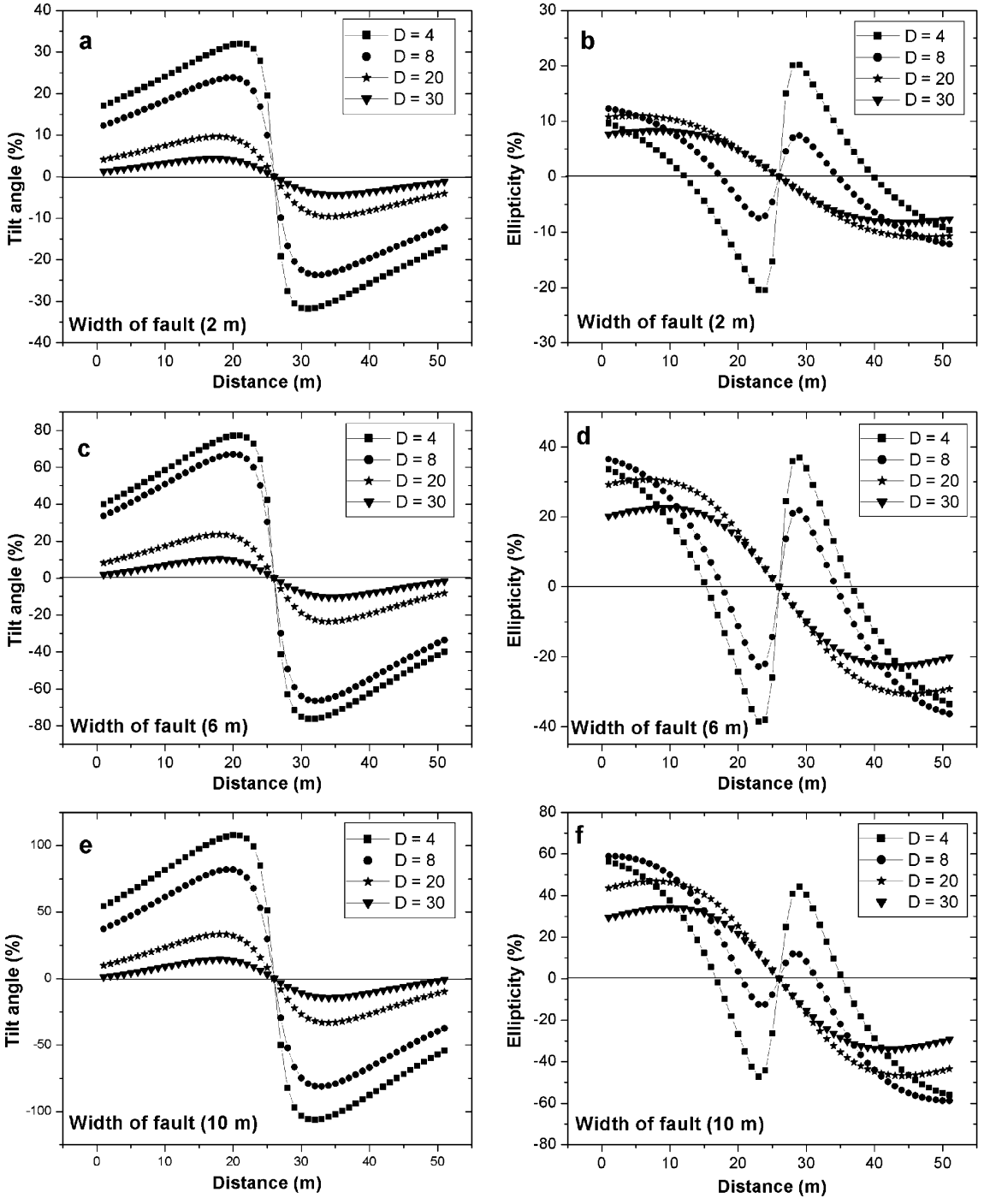

Fig. 14 Theoretical computed VLF curves of a single fracture zone within the basement rock with varying thickness of overburden (*D*). The *left panels* are tilt angle curves while the *right panels* are the corresponding ellipticity curves. In **a** and **b** the fault width is 2 m; in **c** and **d** the fault width is 6 m; and in **e** and **f** the fault width is 10 m

Also, the inversion results corroborate the results from the synthetic simulation which indicates that the existence of basement depression around electrode stations 4 and 7 in line A-A′ and electrode stations 5–8 in line B-B′ possibly suggest the existence of a fault within the basement rock which manifested as a local drop in the resistivity of the basement and thickening of the overburden. According to Olayinka and Barker (1990), such a zone is known to be favourable to groundwater accumulations, since their hydrogeological characteristics such as the hydraulic conductivity and porosity must have been enhanced due to fracturing. It is recommended, therefore, that exploration boreholes should be drilled within this zone.

Fracture zone models of limited depth extent were studied to evaluate the limits of the resolution of the depth extent of the fractured zone images shown in Figs. 9d and

 DOI 10.1007/s10040-006-0051-2

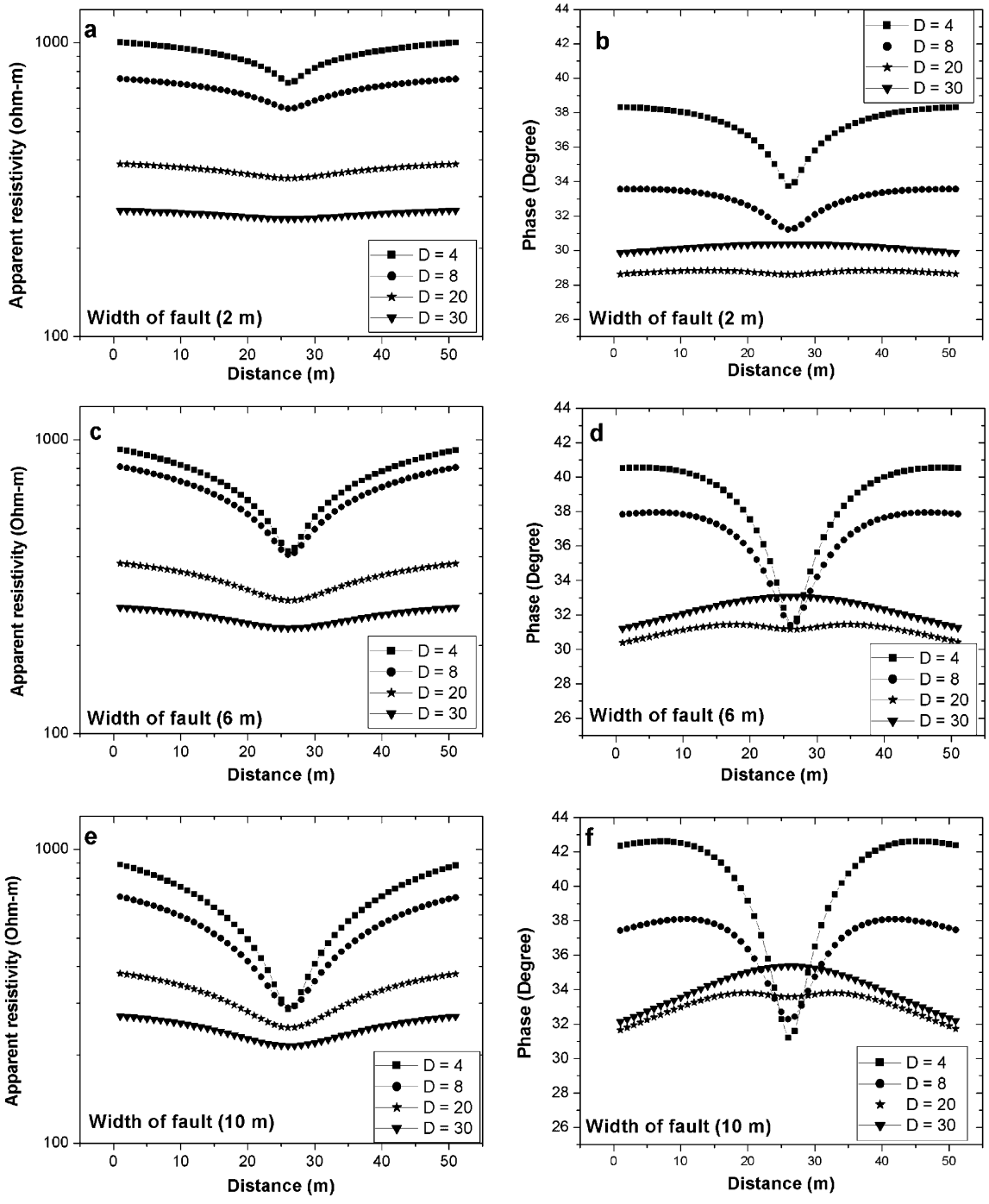

Fig. 15 Theoretical computed VLF-R curves of a single fracture zone within the basement rock with varying thickness of overburden (*D*). The *left panels* are apparent resistivity curves while the *right panels* are the corresponding phase curves. In **a** and **b** the fault width is 2 m; in **c** and **d** the fault width is 6 m; and in **e** and **f** the fault width is 10 m

10d and confirm whether the inverted dipole–dipole data shown were actually detecting the fracture zone or the zone of slightly thicker overburden associated with it. For these particular models, the overburden thickness was fixed at 10 m, while the depth extent of the fracture zone was varied (10, 20, 30 and 40 m, see Fig. 12). A resistivity value of 50 ohm-m and a thickness of 10 m was assigned to the fracture zone. The resistivity of the overburden is represented by 200 ohm-m. The pseudosections computed for the above models show convincing evidence of the existence of the fracture zone as depicted in Fig. 13. From this figure, the RMS error increases as the depth extent increases, indicating that the resolution of the inverted images degrades as the depth extent increases. This result also points to the fact the dipole–dipole method used was actually detecting the fracture zone within the basement and not the zone of slightly thicker overburden associated with it. The presence of the fracture zone caused a local

 DOI 10.1007/s10040-006-0051-2

deepening of the bedrock topography. The local deepening of the bedrock topography which is associated with in situ weathering induced by fracturing increases as the depth extent of the fracture zones increases. The results of these synthetic examples clearly shows that it is really not possible to see the bottom of a fracture zone from the inverted images; its top is well resolved compared to the base. The resolution, vis-à-vis the amplitude of the observed local anomaly seen at the location of the fractured zone is controlled by the width/depth extent ratio of the fracture zone.

Theoretical VLF data

The results of the numerical modelling experiment based on the synthetic resistivity model shown in Figs. 2, 4 and 6 as models 1, 2 and 3 are presented in Figs. 14 and 15 for the VLF and very low frequency resistivity mode (VLF-R) responses, i.e. the apparent resistivity (ρ_a) and phase (ϕ). All results presented in this section were computed using 100 elements in an x direction and 30 elements in a y direction, making a total of 3,000 elements. The length of the modelled survey line was chosen to be 200 m. During this study, the model response of the fracture zone was computed at a fixed frequency of 16 kHz at every 4 m making a total of 51 VLF data points on the profile. In general, a half space having a resistivity of 1,500 ohm-m overlain by an overburden having a resistivity of 200 ohm-m and a vertical fault having a resistivity of 50 ohm-m embedded within the basement was used as the input model. The fracture zone was considered to have a dip angle of 90°. The model closely approximates a geologic situation where the fault has a long strike length. In this study, the effects of varying the overburden thickness and fracture size on the VLF model responses were studied. The model results are shown as tilt angles (Fig. 14a,c,e), ellipticity (Fig. 14b,d,f), apparent resistivity (Fig. 15a,c,e) and phase (Fig. 15b,d,f). Only qualitative interpretation is given to the model results. Figure 14a,c,e displays the tilt angles (θ) plotted against the horizontal distance along the profile. In Fig. 14a,c,e, tilt angle anomaly corresponding to low resistivity that is indicative of a fractured/fault zone is clearly depicted at station 25. In all the model results, the top of the fracture zone is centred at the inflection point of the anomaly. All the tilt angle curves show symmetrical shape that is typical of vertically dipping structures. However, the peak–peak amplitude of the curves decreases as the overburden thickness increases from 4 to 30 m. This shows that the overburden thickness definitely affected the VLF response that was obtained. Also, the amplitude of the tilt angle model response increases significantly as the size of the fracture zone increases from 2 to 10 m. This indicates that the model response is influenced by the size of the fracture zone. That is, a large fracture zone will produce a large amplitude tilt angle response and vice-versa. The shape of the in-phase anomaly is consistent with an anomaly having a small size (w) and also suggests strong contribution from the overburden itself as the overburden thickness increases.

Also, the ellipticity profiles (Fig. 14b,d,f) show strong negative cross-over quadrature anomaly where the in-phase shows positive at station 25. That is, the quadrature component values are of reverse polarity to the real component. The ellipticity curves seem more complex in their behaviour than the tilt angle curves. From the ellipticity curves shown in Fig. 14b,d,f, it is seen that the ellipticity curves are symmetrical. They all depict typical anomaly curves showing relatively strong quadrature components which suggests that the fracture zone is a good conductor and a resistive host rock. However, in all the models, the peak–peak amplitude of the ellipticity curves increases as the fracture zone size decreases, but decreases as the overburden thickness increases. The shape of the quadrature curve is interpreted as being caused almost entirely by the buried conducting fracture zone, as the shape of the quadrature model curves was observed to be strongly affected by the thickness of the overburden. The dip of the conductive fracture zone is also reflected in the quadrature component which shows that the anomaly is vertical dipping (90°). In general, all the synthetic anomaly response curves that were obtained correlate with the field case study that was shown by Paterson and Ronka (1971). The inference drawn from the modelling result is that the model curves obtained are possible representations of real fracture zones occurring in crystalline basement terrain, and having similar geometry and characteristics as the synthetic model. Furthermore, the level of confidence in the model result is high because the Ile-Ife study used a priori geologic and geophysical information that are both available for the study area. In the VLF-R resistivity model data, low resistivity zones were interpreted as a possible fracture zone (Fig. 15a,c,e). A central low resistivity zone is shown at station 25 m irrespective of the overburden thickness. However, when the size of the fracture zone is small compared to the overburden thickness, the response of the resistivity model is almost obscured, but as the size of the fracture zone increases, low resistivity depicting the location of the fracture zone becomes more distinct. The presence of the fault and overburden is shown to significantly alter the phase curves at 20–30 m. Also, phase response decreases for thin overburden thickness and fracture zone size, but the phase curves increased for thick overburden thickness and large fracture zone size (Fig. 15b,d,f). It is thus inferred that the overburden thickness and large fracture zone size are the major factors controlling the resistivity and phase model responses that were obtained (Fig. 15).

Comparison of field and synthetic VLF data

To confirm the accuracy of the predicted model results and demonstrate the efficacy of the modelling program, field VLF measurements were taken along the traverses shown in Fig. 1 and the data compared with the results of the predicted models. That the assumed vertical fault model structure used in this study is consistent with the field data

 DOI 10.1007/s10040-006-0051-2

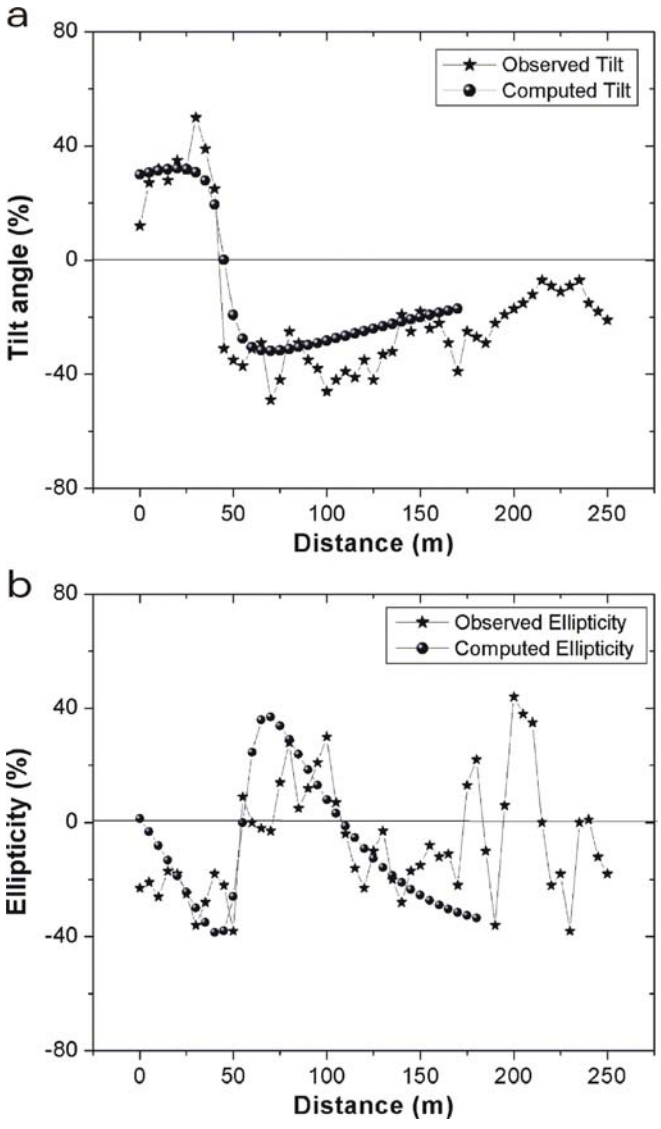

Fig. 16 A comparison of the field VLF data obtained on profile A-A′ and the computed synthetic VLF data showing **a** tilt angle and **b** ellipticity

is evident from the computed and observed responses plotted respectively in Figs. 16 and 17. These figures show the comparison between the observed and computed tilt angle (θ) and ellipticity responses for both profiles A-A′ and B-B′. It is evident from these figures that there is general good agreement between the observed and the computed tilt angle and ellipticity data as both the field and synthetic data fit very well. This comparison shows that the predicted responses for the assumed vertical fault models are consistent with field observations. Furthermore, the symmetrical pattern of the VLF signatures and the crossover of the tilt angle (θ) and ellipticity shown in Figs. 16 and 17 indicate the presence of a vertically dipping conductor beneath the station 110 m on profile A-A′ (Fig. 16a) and 50 m on profile B-B′ (Fig. 17a). Thus the reversal of polarity of the crossover of the ellipticity component (Figs. 16b and 17b) clearly shows that the delineated anomaly beneath this station is a good conductor as predicted by the models. Also, the non-zero high amplitude of the ellipticity obtained on these traverses indicates that the near surface overburden material is moderately conductive while the host rock is resistive.

Conclusion

Two surface geophysical methods (direct current dipole–dipole resistivity and very low frequency electromagnetics) were used to determine the location of a suspected fracture zone in crystalline bedrock that should favour groundwater accumulation. The results obtained from both the synthetic and field data were correlated to locate the fracture zone. A prominent low resistivity anomalous zone was detected with the two geophysical methods employed in this study. The feature is interpreted as a steeply

 DOI 10.1007/s10040-006-0051-2

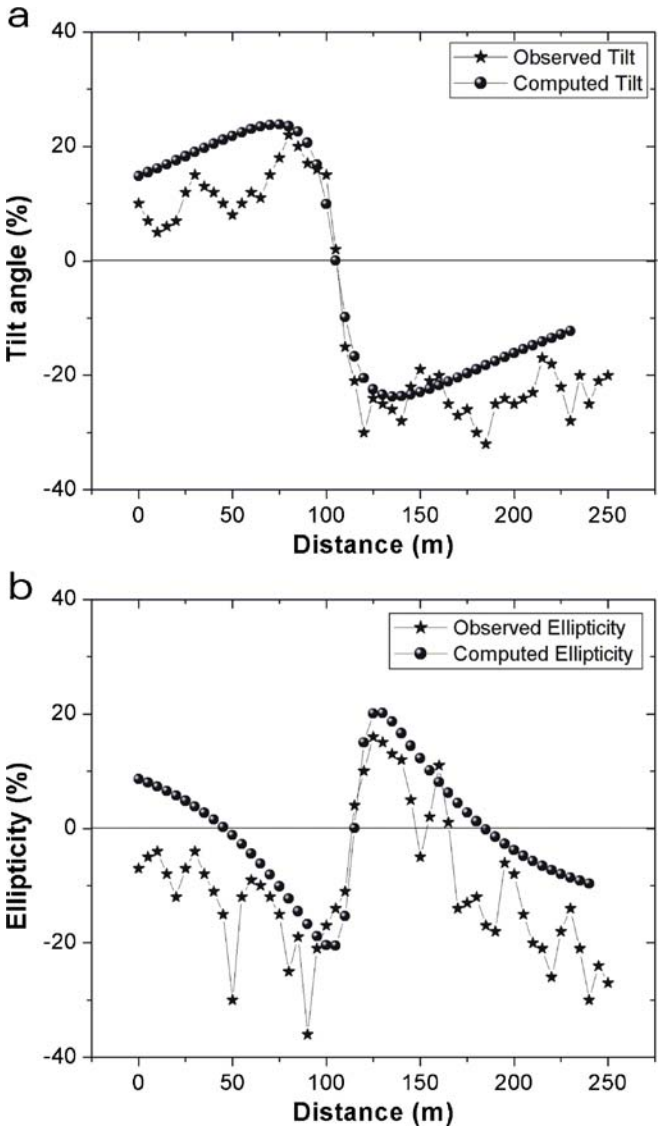

Fig. 17 A comparison of the field VLF data obtained on profile B-B′ and the computed synthetic VLF data showing **a** tilt angle and **b** ellipticity

dipping subvertical fracture zone approximately 10 m wide. The resolution of the subsurface images obtained from the inversion of the synthetic resistivity data increases when the width of the fracture zone is half the thickness of the overlying overburden, but decreases as the thickness of the overburden increases. A good characterization of the fractured bedrock within a basement complex rock of southwestern Nigeria was obtained by the integrated use of two geophysical methods. The results from the field data are in general agreement with the numerical modelling experimental results. The VLF model response cross-over point was shown to correspond to fault location. It was also discovered that large overburden thickness attenuates the VLF responses. Also, from the numerically modelled VLF result, it was observed that as the overburden and fault thickness increases, the peak–peak amplitude of the model response are attenuated and progressively pushed apart from the cross-over point. Also, the sign of the model responses changed right on top of the fracture zone location. The VLF-EM method was established as being a very important tool in delineating faults that may act both as pathways for groundwater movements in the basement rocks and be indirect indicators of the rock mass quality index. It was suggested, therefore, that before embarking on borehole siting in hard-rock terrains, a preliminary reconnaissance geophysical survey using electrical resistivity or VLF technique should first be conducted to estimate the overburden thickness and identify those promising areas having low resistivity within the basement that will be recommended for further detailed geophysical survey before drilling is carried out. Secondly, the reconnaissance survey should be followed by a detailed dipole–dipole survey across promising areas. In doing this, the risk of drilling low-yield water wells will be significantly reduced.

 DOI 10.1007/s10040-006-0051-2

Acknowledgements The numerical modelling and inversion was carried out in the Geoelectrical Imaging Laboratory, Korea Institute of Geoscience and Mineral Resources, Daejeon, South Korea. The first author is grateful to the South Korean government for granting him a post-doctoral fellowship that enabled him to carry out the research. Shell Petroleum Development Company of Nigeria provided the financial assistance for the fieldwork to Professor B.D. Ako.

References

Acworth RI (1987) The development of crystalline basement aquifers in a tropical environment. Q J Eng Geol 20:265–272

Adepelumi AA, Ako BD, Ajayi TR (2001) Groundwater contamination in the basement-complex area of Ile-Ife, SW Nigeria: a case study using the electrical-resistivity geophysical method. Hydrogeol J 9:611–622

Ajayi TR, Adepelumi AA (2002) Reconnaissance soil-gas radon survey over the faulted crystalline area of Ile-Ife, Nigeria. Environ Geol 41:608–613

Ajibade AC, Woakes M, Rahaman MA (1987) Proterozoic crustal development in the Pan-African regime of Nigeria. In: Kroner A (ed) Proterozoic lithoshperic evolution, vol 17. American Geophysical Union, Washington, DC, pp 259–271

Apparao A, Roy A (1971) Resistivity model experiments II. Geoexploration 9:195–205

Barker RD (1999) Surface and borehole geophysics. In: Lloyd JW (ed) Hardrock aquifers. UNESCO, Paris

Barker RD, White CC, Houston JFT (1992) Borehole siting in an African accelerated drought relief project In: Wright EP, Burgess WGE (eds) Hydrogeology of crystalline basement aquifers in Africa, Geological Society Special Publication, No. 66, London, pp 183–201

Carruthers RM, Smith IF (1992) The use of ground electrical survey methods for siting water-supply boreholes in shallow crystalline basement terrains. In: Wright EP, Burgess WGE (eds) Hydrogeology of crystalline basement aquifers in Africa. Geological Society Special Publication, No. 66, London, pp 203–220

Kaikkonen P (1980) Interpretation nomograms for VLF measurements. Acta Uni Oul A 92 Phys 17:1–48

Kaikkonen P, Sharma SP (1997) Delineation of near-surface structures using VLF and VLF-R data: an insight from the joint inversion results. Leading Edge 16:1683–1686

KIGAM (2001) DIPRO version 4.01, Processing and interpretation software for electrical resistivity data. KIGAM, Daejeon, South Korea

KIGAM (2002) EM2Dmodel version 1.0, Processing and interpretation software for electrical resistivity data. KIGAM, Daejeon, South Korea

Lohman SW (1972) Ground-water hydraulics. Prof Paper No. 708, US Geol Surv, Reston, VA, pp 1–70

McNeill JD (1990) Use of electromagnetic methods for groundwater studies. In: Ward SH (ed) Geotechnical and environmental geophysics, vol 1. Soc Expl Geophys, Tulsa, OK, pp 191–218

McNeill JD, Labson VF (1991) Geological mapping using VLF radio fields. In: Nabighian M (ed) Electromagnetic methods in applied geophysics, vol 2, part B. Soc Expl Geophys, Tulsa, OK, pp 521–640

Medeiros WE, Lima OAL (1990) A geoelectrical investigation for ground water in crystalline terrains of Central Bahia, Brazil. Ground Water 28:518–523

Okhue ET, Olorunfemi MO (1992) Electrical resistivity investigation of a typical basement complex area. J Mining Geol 2:63–68

Olayinka AI, Barker R (1990) Borehole siting in crystalline basement areas of Nigeria with a microprocessor-controlled resistivity traversing system. Ground Water 28:178–183

Olayinka AI, Weller A (1997) The inversion of geoelectrical data for hydrogeological application in crystalline basement areas of Nigeria. J Appl Geophys 37:103–115

Palacky GJ, Ritsema IL, de Jong J (1981) Electromagnetic prospecting for groundwater in Precambrian terrains in the Republic of Upper Volta. Geophys Prospect 29:932–955

Paterson NR, Ronka V (1971) Five years of surveying with the very low frequency electromagnetic method. Geoexploration 9:7–26

Rahaman MA (1988) Recent advances in the study of the basement complex of Nigeria. In: Oluyide PO et al (eds) Precambrian geology of Nigeria. Geological Survey of Nigeria, Kaduna, pp 11–43

Saydam AS (1981) Very low frequency electromagnetic interpretation using tilt angle and ellipticity measurements. Geophysics 46:1594–1605

Seaton WJ, Burbey TJ (2002) Evaluation of two-dimensional resistivity methods in a fractured crystalline-rock terrain. J Appl Geophys 51:21–41

Singh KP (2005) Non-linear estimation of aquifer parameters from surficial resistivity measurements. Hydrol Earth Syst Sci Discuss 2:917–938

Sinha AK (1990) Interpretation of ground VLF-EM data in terms of vertical conductor models. Geoexploration 26:213–231

Smith BD, Ward SH (1974) On the computation of polarization ellipse parameters. Geophysics 39:867–869

van der Kamp G (2001) Methods for determining the in situ hydraulic conductivity of shallow aquitards: an overview. Hydrogeol J 9:5–16

Yi MJ, Kim JH, Chung SH (2003) Enhancing the resolving power of least-squares inversion with active constraint balancing. Geophysics 68:931–941